Seismic metamaterials: Generating low-frequency bandgaps induced by inertial amplification

Yi Zeng, Liyun Cao, Sheng Wan, Tong Guo, Yan-Feng Wang, Qiu-Jiao Du, Badreddine Assouar, Yue-Sheng Wang

Seismic metamaterials: Generating low-frequency bandgaps induced by inertial amplification

Yi Zeng[1, 2], Liyun Cao[2], Sheng Wan[2], Tong Guo[2], Yan-Feng Wang[1], Qiu-Jiao Du[3], Badreddine Assouar[2, *] and Yue-Sheng Wang[1, 4, *]

[1] *Department of Mechanics, School of Mechanical Engineering, Tianjin University, Tianjin 300350, China*

[2] *Université de Lorraine, CNRS, Institut Jean Lamour, Nancy 54000, France*

[3] *School of Mathematics and Physics, China University of Geosciences, Wuhan 430074, China*

[4] *Department of Mechanics, Beijing Jiaotong University, Beijing 100044, China*

* Electronic mail: badreddine.assouar@univ-lorraine.fr (B. Assouar), yswang@tju.edu.cn (Y.-S. Wang).

Abstract

In the last two decades, seismic metamaterials have attracted significant attention of researchers because of the characteristic of the bandgap which can be used to control seismic surface waves. The inertial amplification mechanism has been used to design metamaterials capable of isolating elastic waves in rods, beams, and plates at low frequencies. In this work, we propose an alternative type of seismic metamaterial with a low-frequency bandgap induced by inertial amplification for isolating seismic surface waves. The characteristics of the bandgap induced by inertial amplification are experimentally demonstrated by using a metamaterial plate composed of 25 unit cells. The propagation of the flexural waves imaged by scanning laser Doppler vibrometer shows strong attenuation effects induced by the metamaterial plate in the bandgap. The

broadband attenuation is investigated by using two kinds of unit cells. Finally, similar structures with inertial amplification are introduced to design the seismic metamaterials to isolate seismic surface waves at low frequencies.

Keywords: seismic metamaterials; bandgap; surface waves; inertial amplification

1. Introduction

Seismic Rayleigh waves at the frequencies below 20 Hz are the greatest threat to the man-made buildings located in the mid and far fields of the seismic source when earthquakes happen [1, 2]. Seismic metamaterials (SMs) [2-11] have been proposed by researchers to isolate the seismic Rayleigh waves before they arrive the critical infrastructures and buildings. This is due to the bandgap characteristics of the SMs composed of the periodic arrangement of artificial unit cells. The seismic waves will be attenuated significantly by the SMs in the frequency range of the bandgap [12-20].

In 1999, the experiments [21] in a marble with prepared phononic crystals constituted of a periodic array of cylindrical holes showed the existence of the bandgaps for the surface waves. Therefore, the possible applications were obtained to attenuate seismic surface waves. During the last two decades, various kinds of SMs [4, 22-31] have been designed to isolate surface waves in seismic movements, especially at low frequencies. It is worth mentioning that the plate model was validated to open an attenuation zone (AZ) around 50 Hz by using large-scale experiments on the phononic crystal in the ground [6]. This work demonstrated that the SMs have the ability to attenuate the propagation and control the transmission of the elastic waves in the earth's surface, although the working frequency is not low enough in the experiments. Therefore, when researchers found that the forests can attenuated seismic waves in earthquakes, the SMs constituted of an array of pillars on a soil substrate were proposed to achieve low-frequencies bandgap based on the local resonance of the pillars [7, 32-34]. In addition, for better integration of SMs in the foundation of a building for seismic isolation

purposes, Yan et al. [35] proposed a 2D periodic foundation constituted of ductile cast iron, supper soft rubber and reinforced concrete, while Casablanca et al. [36] designed a periodic mass-in-mass foundation placed underneath buildings. To obtain wider bandgaps, the pillars with different kinds of structures [28, 37-42], and the “rainbow trapping effects” [8, 29, 34, 43-47] were utilized. However, the ultra-low-frequency (< 2 Hz) bandgaps are hard to obtain by using small-size structures.

Fortunately, the inertial amplification proposed by Yilmaz et al. [48-50], which induces low-frequency bandgaps by using a small mass, was utilized to design metamaterials. The lever-arm structures were introduced to amplify the motion of the resonate small mass, which in turn effectively reduces the resonance frequency. Based on the similar structures, Li et al. [51] proposed a phononic beam to isolate transverse waves utilizing inertial amplification resonators. A wide bandgap induced by inertial amplification in a continuous elastic rod was obtained and a general 2D realization of the inertially amplified system in a plate was proposed in Ref. [52]. In addition, Acar et al. [53] experimentally and numerically proposed a periodic solid structure which exists wide and deep bandgaps induced by embedded inertial amplification mechanisms. The 3D structures was experimentally demonstrated by using embedded inertial amplification mechanisms, which can isolate elastic waves in a wide frequency range [54]. Recently, a 2D solid structure with embedded inertial amplification mechanisms was designed by using topology optimization to obtain an ultrawide bandgap at low frequencies [55]. To enlarge the bandwidth of the bandgap and the specific stiffness simultaneously, Mizukami et al. [56] proposed an inertial amplification-type metamaterial by using

continuous carbon fibers. Furthermore, the rotary motion conversion mechanism of an inertial amplification of continuous structure was used to generate a wide bandgap at low frequencies [57]. A four-bar inertial amplification mechanism on corrugated-core sandwich panels was proposed to achieve strong vibration attenuation in the range of low frequencies [58]. However, there is almost no research of the SMs with inertial amplification to achieve the low-frequency bandgaps for surface waves.

In this work, we propose a kind of the SM with a low-frequency bandgap induced by inertial amplification to attenuate seismic surface waves. We first experimentally demonstrate the bandgap characteristics of inertial amplification effects in a metamaterial plate (MMP) sample formed by 5×5 periodic unit cells. The band structure of the simplified model of the MMP is also analytically calculated by using the transfer-matrix method. Then, to achieve the broadband attenuation, two kinds of unit cells with different positions of hinge joints are chosen to construct a new complex metamaterial plate (CMP). Finally, the inertial amplification mechanisms are introduced to design the SMs which are capable of isolating seismic surface waves at low frequencies. It is very known that inertial amplification mechanisms with small mass can achieve strong vibration attenuation at low frequencies, which property the SMs most need. This work demonstrates that the inertial amplification mechanisms can also induce the bandgap for seismic surface waves at ultra-low frequencies even with using the simple structures.

2. Method and Models

Figure 1(a) illustrates the unit cell of the MMP based on inertial amplification in the

experiments and utilized in the simulation calculations. The simplified model of the structure is also given in Fig. 1(b). The unit cell is constituted of the lever, the support bar, mass, spring, hinge joint and the base plate. In the MMP, the lattice constant a is 3 cm. The thickness t of the plate is 1 mm. The other geometric parameters of the structure are shown in Fig. 1(c). The resonant frequency of the resonator in the model is [48, 59]

$$f = \frac{1}{2\pi}\sqrt{\frac{k}{(\mu-1)^2 m}}\ , \tag{1}$$

where $\mu = l_1/\ l_2$ is the lever ratio with l_1 being the length of the lever and l_2 being the distance between the spring and support bar; k is the stiffness of the spring; and m is the mass. The inertial mass will be amplified $(\mu\text{-}1)^2$ times and the resonance frequency will be reduced $(\mu\text{-}1)$ times when the lever is rigid and has no mass. A low resonance frequency f can be achieved in the following cases. First, when the stiffness of the spring k is small, which means the soft material is used. Second, when the lever ratio μ is large, which means the long lever (i.e., l_1 is large) is used or the position of the support bar is near the spring (i.e., l_2 is small). Third, when large mass (i.e., m is large) is used. Therefore, there are a lot of options to design elastic metamaterials with low-frequency bandgaps, including SMs which we will mention later.

Figure 1(d) illustrates the experimental sample of the MMP. The sample is formed by 5 ×5 periodic unit cells. In this sample, all parts are printed using 3D printer. The PLA rod is fabricated and the lever and the support bar are assembled with PLA rod horizontally installed through the holes to form the hinged part. More enlarged photograph of the hinged part can be found in Appendix A. The source vibrating in z direction is excited at one end of the MMP. Figure 1(e) shows the experimental layout.

Label A is a computer, which is utilized to set the output signal of the source on sample B and processes the input signal from the laser vibrometer C. In order to obtain clear and perfect propagation effects of flexural waves in the MMP, the laser vibrometer (Polytec PSV-500) is used to measure on the back of the MMP. In addition, a bare plate D, which is the same plate as in the MMP, is also measured to provide the control results.

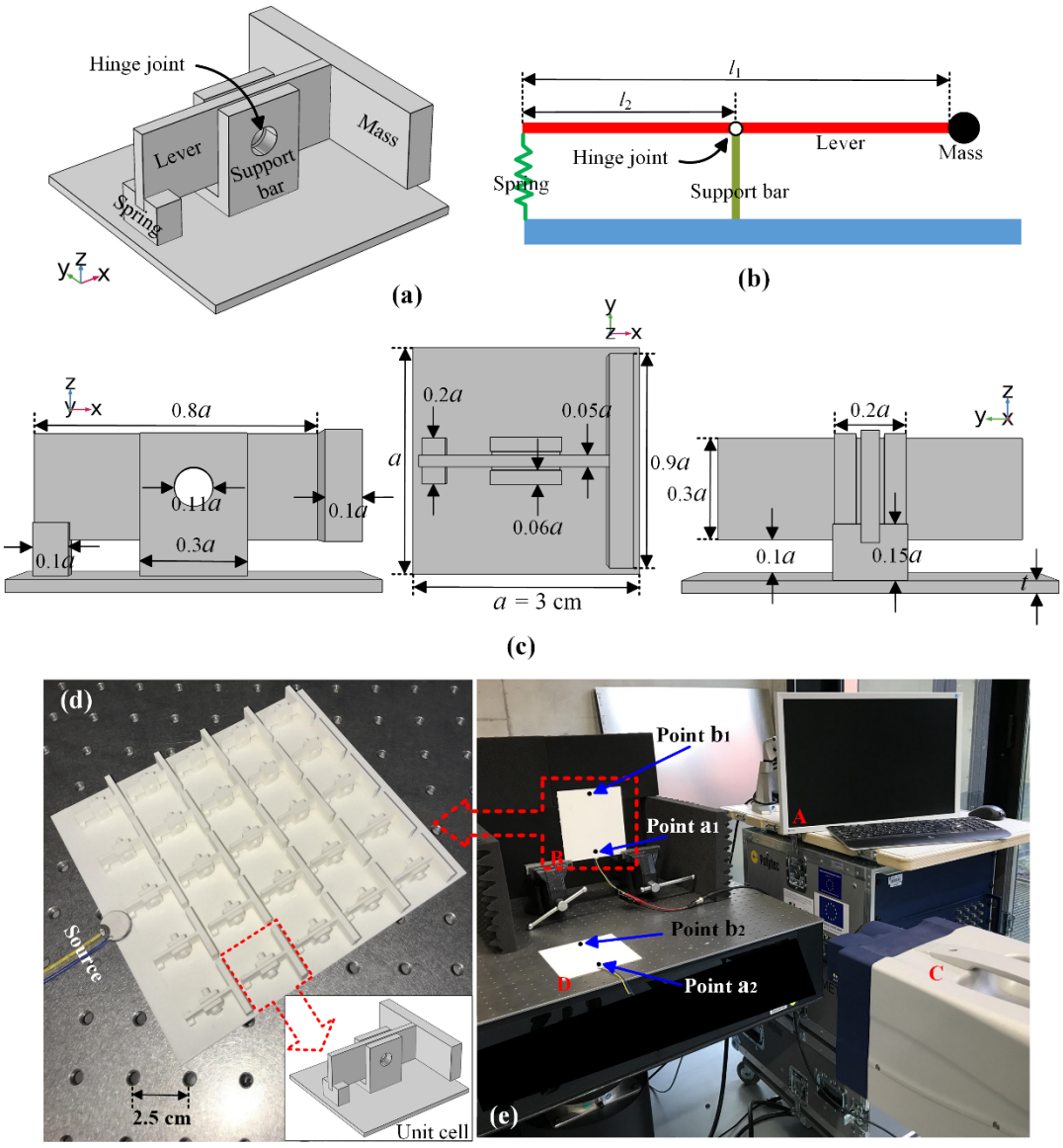

Figure 1 (a) The unit cell of the MMP considered in the numerical simulation and experiment. (b) The simplified model of the (a). (c) The geometric parameters of the unit cell. (d) The experimental sample of the MMP and (e) the experimental layout with a computer (Label A), the MMP (Label B),

the laser vibrometer (Label C) and the same plate (Label D) as in the MMP.

In order to facilitate the realization of the 3D printing of the MMP, the material of the whole structure is chosen as PLA whose Young's modulus is 3.4398 GPa, density is 1086.3 kg/m^3, and Poisson's ratio is 0.35 in the both simulation and experiment [60]. The connections between the support bar and the base plate, the base plate and the spring, the lever and the mass are perfect continuous. The spring and the lever are perfectly glued together. It is worth noting that the material of the spring part is PLA. Of course, according to the Eq. (1), the spring part can be replaced by a softer material to obtain a less k and a lower-frequency bandgap. The connection between the lever and the support bar is hinge joint. The thickness of the lever along z axis is set as $0.3a$ to enhance the bending stiffness of the lever along z axis. At low frequencies, the lever can be regarded as a rigid part to achieve the inertial amplification.

The simulation results in this work are all calculated by using the multibody dynamics module of COMSOL 5.4. The periodic boundary conditions are set on the plate of the unit cell along x and y directions. It is worth noting that both boundary similarity and pointwise constraint are utilized to achieve the periodic boundary condition in the multibody dynamics module. The hinge joint between the lever and the support bar shown in Fig. 1 is set as hinge-connection condition.

The same structure as the experimental sample shown in Fig. 1(d) is used in simulation of the flexural wave propagation in the MMP. The transmission spectrums in the experiments and simulations are all defined as

$$TS = 20 \times \log_{10}(R_1/R_0), \tag{2}$$

where R_0 and R_1 are the root mean square (RMS) of the out-of-plane velocities at the two points a_1 (a_2) and b_1 (b_2) shown in Fig. 1(d), respectively.

3. Analytical solutions of the simplified model

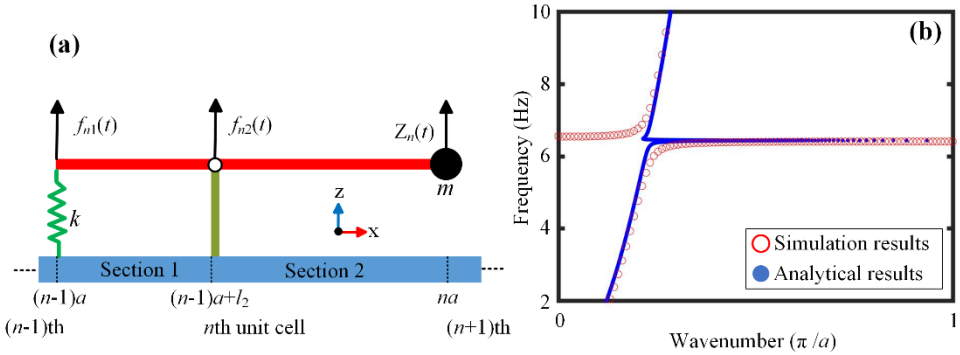

Figure 2 (a) The simplified model used for analytical solution. (b) the numerical simulation results (COMSOL) and analytical results of the band structure of the simplified model.

The transfer-matrix method can be used to analytically calculate the band structure of the one-dimensional periodic simplified model. As shown in Fig. 2(a), the simplified model used for analytical solution can be assumed as the Euler-Bernoulli beam with inertial amplified resonators. So, the governing equation for the flexural waves in the beam is

$$EI\frac{\partial^4 z(x,t)}{\partial x^4} + \rho A\frac{\partial^2 z(x,t)}{\partial t^2} = 0, \tag{3}$$

where E, I, ρ and A are Young's modulus, section moment of inertia, density and section area of the beam, respectively. $z(x,t)$ is the out-plane displacement of the beam. The physical quantities of the beam can be expressed in the following forms [61]:

$$z(x,t) = \left(Ae^{-i\lambda x} + Be^{i\lambda x} + Ce^{-\lambda x} + De^{\lambda x}\right)e^{i\omega t}, \tag{4}$$

$$\theta(x,t) = y(x,t)', \tag{5}$$

$$M(x,t) = EIy(x,t)'', \tag{6}$$

$$Q(x,t) = -EIy(x,t)''', \tag{7}$$

where A, B, C and D are complex coefficients; $\lambda = \sqrt[4]{\rho A\omega^2/EI}$ with $\omega = 2\pi f$ being the circular frequency is the flexural wavenumber; and θ, M and Q are the slope, bending moment and shear force, respectively.

In the nth unit cell, the out-plane displacement of section 1 is

$$z_{n,1}(x_1,t) = \left(A_{n,1}e^{-i\lambda x_1} + B_{n,1}e^{i\lambda x_1} + C_{n,1}e^{-\lambda x_1} + D_{n,1}e^{\lambda x_1}\right)e^{i\omega t}, \tag{8}$$

where $x_1 = x - (n-1)a$ and $(n-1)a \le x \le (n-1)a + l_2$. So, from the left side to the right side of section 1 of the nth unit cell, we obtain the transfer matrix in this field by following:

$$\mathbf{\Psi}_{n,1}(0,t) = \mathbf{H}_{1\alpha}\left[A_{n,1}\ B_{n,1}\ C_{n,1}\ D_{n,1}\right]^T e^{i\omega t}, \tag{9}$$

$$\mathbf{\Psi}_{n,1}(l_2,t) = \mathbf{H}_{1\beta}\left[A_{n,1}\ B_{n,1}\ C_{n,1}\ D_{n,1}\right]^T e^{i\omega t}, \tag{10}$$

where $\mathbf{\Psi}(x,t) = [z(x,t)\ \theta(x,t)\ M(x,t)\ Q(x,t)]^T$ is the state vector; and $\left[A_{n,1}\ B_{n,1}\ C_{n,1}\ D_{n,1}\right]^T$ is the coefficient vector. Substituting Eq. (10) into Eq. (9), we obtain

$$\mathbf{\Psi}_{n,1}(l_2,t) = \mathbf{H}_{1\beta}\mathbf{H}_{1\alpha}^{-1}\mathbf{\Psi}_{n,1}(0,t) \triangleq \mathbf{H}_1\mathbf{\Psi}_{n,1}(0,t), \tag{11}$$

where $\mathbf{H}_1$ is the transfer matrix. It is shown in Appendix B.

Similarly, the out-plane displacement of section 2 is

$$z_{n,2}(x_2,t) = \left(A_{n,2}e^{-i\lambda x_2} + B_{n,2}e^{i\lambda x_2} + C_{n,2}e^{-\lambda x_2} + D_{n,2}e^{\lambda x_2}\right)e^{i\omega t}, \tag{12}$$

where $x_2 = x - (n-1)a$ and $(n-1)a + l_2 \le x \le na$. So, from the left interface to the right one of section 2 of the nth unit cell, we obtain

$$\mathbf{\Psi}_{n,2}(a,t) = \mathbf{H}_{2\beta}\mathbf{H}_{2\alpha}^{-1}\mathbf{\Psi}_{n,2}(l_2,t) \triangleq \mathbf{H}_2\mathbf{\Psi}_{n,2}(l_2,t), \tag{13}$$

where $\mathbf{H}_2$ is the transfer matrix. It is shown in Appendix B.

As for the *n*th lever-arm structure on the beam, the dynamic equilibrium equation is

$$f_{n1}(t) + f_{n2}(t) + m\ddot{Z}_n(t) = 0, \tag{14A}$$

$$l_2 f_{n1}(t) + (l_1 - l_2)m\ddot{Z}_n(t) = 0, \tag{14B}$$

where $Z_n(t)$ is the displacement of the *n*th mass of the lever-arm structure; and $f_{n1}(t)$ and $f_{n2}(t)$ are the forces of the spring and support bar on the lever, respectively. Due to the Hooke's Law, we obtain

$$f_{n1}(t) = k\left[\frac{Z_n(t)}{\mu-1} + z_{n,1}(0,t) - z_{n,2}(l_2,t)\right], \tag{15}$$

where k is the spring stiffness; and $\mu = l_1/l_2$ is lever ratio. Substituting Eq. (15) into Eq. (14), we obtain

$$f_{n1}(t) = \frac{kmw^2(\mu-1)^2}{mw^2(\mu-1)^2-k}[z_{n,1}(0,t) - z_{n,2}(l_2,t)] \triangleq G_1[z_{n,1}(0,t) - z_{n,2}(l_2,t)], \tag{16}$$

$$f_{n2}(t) = \frac{kmw^2(-\mu^2+3\mu-2)}{mw^2(\mu-1)^2-k}[z_{n,1}(0,t) - z_{n,2}(l_2,t)] \triangleq G_2[z_{n,1}(0,t) - z_{n,2}(l_2,t)]. \tag{17}$$

Due to the continuities at the interface between (n - 1)th and nth unit cells, we obtain

$$z_{n-1,2}(a,t) = z_{n,1}(0,t), \tag{18A}$$

$$\theta_{n-1,2}(a,t) = \theta_{n,1}(0,t), \tag{18B}$$

$$M_{n-1,2}(a,t) = M_{n,1}(0,t), \tag{18C}$$

$$Q_{n-1,2}(a,t) = Q_{n,1}(0,t) - f_{n1}(t). \tag{18D}$$

Substituting Eq. (16) into Eq. (18), we obtain

$$\mathbf{\Psi}_{n-1,2}(a,t) = \mathbf{H}_3\mathbf{\Psi}_{n,1}(0,t) + \mathbf{H}_4\mathbf{\Psi}_{n,2}(l_2,t), \tag{19}$$

where $\mathbf{H}_3$ and $\mathbf{H}_4$ are shown in Appendix B. Due to the continuities at the interface between sections 1 and 2 of the *n*th unit cell, we obtain

$$z_{n,1}(l_2,t) = z_{n,2}(l_2,t), \tag{20A}$$

$$\theta_{n,1}(l_2,t) = \theta_{n,2}(l_2,t), \tag{20B}$$

$$M_{n,1}(l_2,t) = M_{n,2}(l_2,t), \tag{20C}$$

$$Q_{n,1}(l_2,t) = Q_{n,2}(l_2,t) - f_{n2}(t). \tag{20D}$$

Substituting Eq. (17) into Eq. (20), we obtain

$$\mathbf{\Psi}_{n,1}(l_2,t) = \mathbf{H}_5\mathbf{\Psi}_{n,2}(l_2,t) + \mathbf{H}_6\mathbf{\Psi}_{n,2}(0,t), \tag{21}$$

where $\mathbf{H}_5$ and $\mathbf{H}_6$ are shown in Appendix B. Substituting Eqs. (11), (13), (19) and (21), the transfer equation of the flexural waves from the right interface of the (n - 1)th unit cell to the right interface of the nth unit cell is obtain

$$\mathbf{\Psi}_{n,2}(a,t) = \mathbf{T}_{unit}\mathbf{\Psi}_{n-1,2}(a,t), \tag{22}$$

where $\mathbf{T}_{unit} = \{\mathbf{H}_3\mathbf{H}_1^{-1}[(\mathbf{I}_\mathrm{A} - \mathbf{H}_6\mathbf{H}_1^{-1})^{-1}\mathbf{H}_5\mathbf{H}_2^{-1}] + \mathbf{H}_4\mathbf{H}_2^{-1}\}^{-1}$ is the transfer matrix in which $\mathbf{I}_\mathrm{A}$ is a 4×4 identity matrix.

Considering the Bloch-Floquet theory, we obtain

$$\mathbf{\Psi}_{n,2}(a,t) = e^{iqa}\mathbf{\Psi}_{n-1,2}(a,t), \tag{23}$$

where q is the wavenumber. Substituting Eq. (23) into Eq. (22), we obtain

$$\left|\mathbf{T}_{unit} - e^{iqa}\mathbf{I}_\mathrm{A}\right| = 0. \tag{24}$$

By solving the eigenvalue equation, the band structure can be obtained [62].

For instance, Fig. 2(b) shows the simulated results and analytical results of the band structure of the simplified model, when the lattice constant is a = 1 m; the height, breadth, sectional area, section moment of inertia, Young's modulus and density of the beam is h = 0.05 m, b = 1 m, $A = bh$, $I = bh^3/12$, 207 GPa and 7784 kg/m^3, respectively; l_1 = 0.9 m, l_2 = 0.3 m; m = 15.2838 kg and k = 100,000 N/m. It is worth noting that the support bar and the lever are rigid. The simulation results are calculated by COMSOL

5.4 (Multibody Dynamics Module) to evaluate the accuracy of the analytical solution. The simulated results are almost in agreement with the analytical results, especially for the position of the bandgap. It is worth noting that the frequencies of the two bandgaps are consistent with the predicted result from Eq. (1). Obviously, the frequency of the bandgap can be controlled easily in this model by changing one or more parameters of the structure. For instance, an ultra-low frequency bandgap can be achieved when the mass m or lever ratio μ is larger, or when the spring stiffness k is smaller than the example shown in Fig.2.

4. Results and Discussions of the MMPs

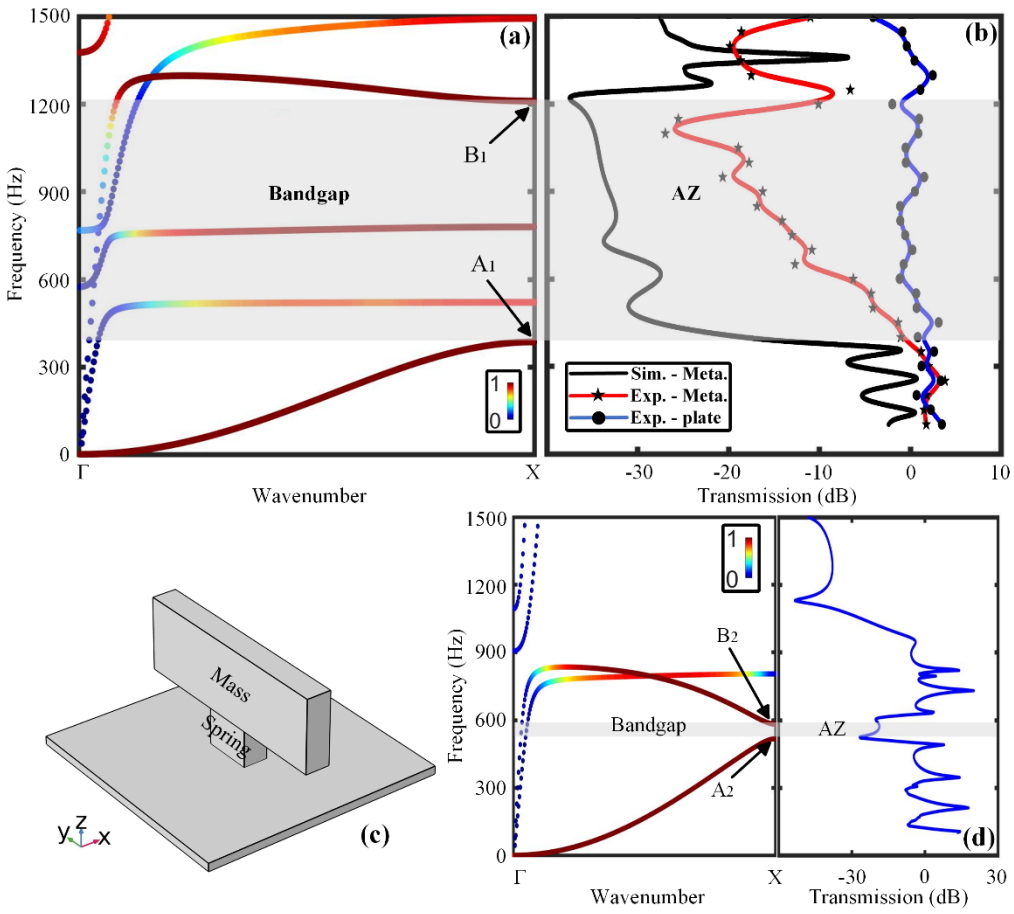

Figure 3 (a) The band structure of the MMP along the ΓX direction. (b) The transmissions of the flexural waves in the MMPs and the bare plate along the ΓX direction. (c) The unit cell consisted of

the same plate, spring and mass as in MMP. (d) The band structure and transmission of the metamaterial constituted of periodic (c). The color bar represents the degree of the out-of-plane polarization (the displacement along the *z* axis). The AZ is attenuation zone.

Figure 3 shows the band structure of the MMP and the transmission of the flexural waves in the MMP and the bare plate along the ΓX direction (i.e. *x* direction). In Fig. 3(a), the out-of-plane polarization in the band structure of the MMP is given. The parameter of the out-of-plane polarization ξ is defined as

$$\xi = \int_S |w|^2 ds \,/\, \int_S (|u|^2 + |v|^2 + |w|^2) dS, \tag{25}$$

where *u*, *v* and *w* are the displacement components in the three directions (*x*, *y* and *z*); and *S* is the whole unit cell. A wide bandgap for the flexural waves can be found from 385 to 1200 Hz. It is worth noting that, the end parts of the second and third dispersion curves have high out-of-plane polarization value. However, these two bands almost do not affect the wide bandgap in Fig. 3(a). We can easily find these two bands are almost flat, especially when out-of-plane polarization value is large. It means it is just the local resonance at a single frequency, which can be ignored when we determine the bandgap. The vibration modes at these two bands are illustrated in Appendix C. As shown in Fig. 3(b), there is a significant AZ at these frequencies in the simulated and experimental results. Compared with the simulated results, the attenuation effects in the experimental results are not particularly obvious at low frequencies in the bandgap. In addition, in the whole bandgap, the attenuation effects in the experimental results are weaker than those in the simulated results. This is due to the fact that the hinge joint in the

experiments is not completely perfect like how it is considered in the simulation. In the experiments, the friction and backlash in the hinged part are difficult to eliminate. Instead, in the simulations, all boundaries in the hinge joint are rigid and smooth. However, it is easy to find that the MMP in the experiments can obviously attenuate the flexural waves in the bandgap compared with the bare plate. For a better comparison, as shown in Fig. 3(c), a periodic structure composed of the same plate, springs and masses as in the MMP is considered. In the band structure and the transmission of the metamaterial, the first bandgap and AZ is very narrow and its lowest frequency is around 520 Hz in Fig. 3(d). In Fig. 1, the lever ratio μ of the proposed unit cell is about 2, so the bandgap range of the inertial amplification mechanism is similar to the that of the spring-mass structure in Fig. 3(c). When the position of the support bar is near the spring, which means the l_2 becomes smaller and μ becomes larger, the bandgap range significantly reduces.

The vibration modes at the marked points in the band structures are illustrated in Fig. 4. Points A_1 (A_2) and B_1 (B_2) are the two boundaries of the bandgaps shown in Figs. 3(a) and 3(d). Figure 4(a) shows the strong resonance of the mass at point A_1. At point B_1, most of the displacement is around the spring part shown in Fig. 4(b). It is clear that the large bandgap is due to the inertial amplification system and the strong resonance of the mass. In Fig. 4(c), most of the displacement is only at the top of the mass, which increases the frequency of the bottom boundary of the first bandgap. In addition, the strong resonance of the mass shown in Fig. 4(d) reduces the frequency of the top boundary of the first bandgap. Therefore, in Fig. 3(d), the frequency of the first bandgap

is higher and the width of the first bandgap is narrower than that in Fig. 3(a).

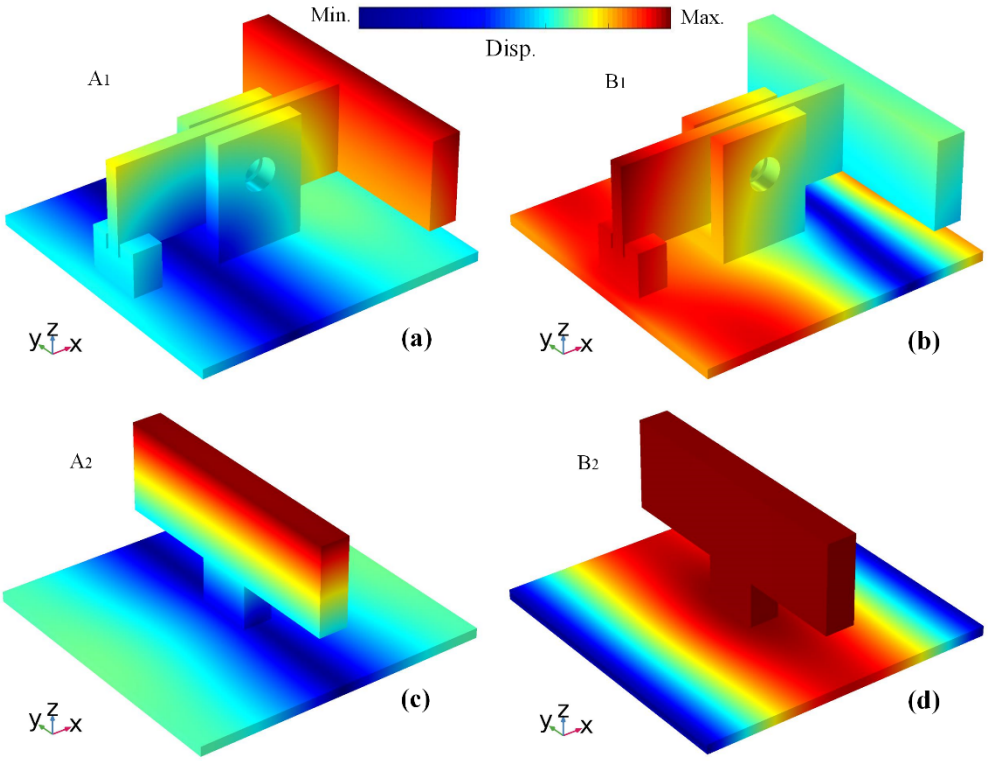

Figure 4 Vibration modes corresponding to points (a) A_1, (b) B_1, (c) A_2 and (d) B_2 marked in Figs. 3(a) and 3(d). The color bar represents the degree of displacement.

The velocity fields of the flexural waves on the back side of the MMP and bare plate were experimentally measured. At 750 Hz, for instance, the results are shown in Figs. 5(a) and 5(b). It is easy to distinguish the attenuation and propagation of the flexural waves in the MMP and bare plate, respectively. In addition, the time-velocity curves for points a_1 and a_2 near the source and points b_1 and b_2 far away from the source are illustrated in Figs. 5(c) and 5(d). Comparing with the vibrations at points a_1 and b_1, we can find that the flexural waves are strongly attenuated in the MMP. Because there is no damping at the boundaries of the plate, the reflected waves can be found from Fig. 5(d). Therefore, the velocity of point b_2 is larger than that of point a_2. The results also

demonstrate the strong attenuation ability of the MMP.

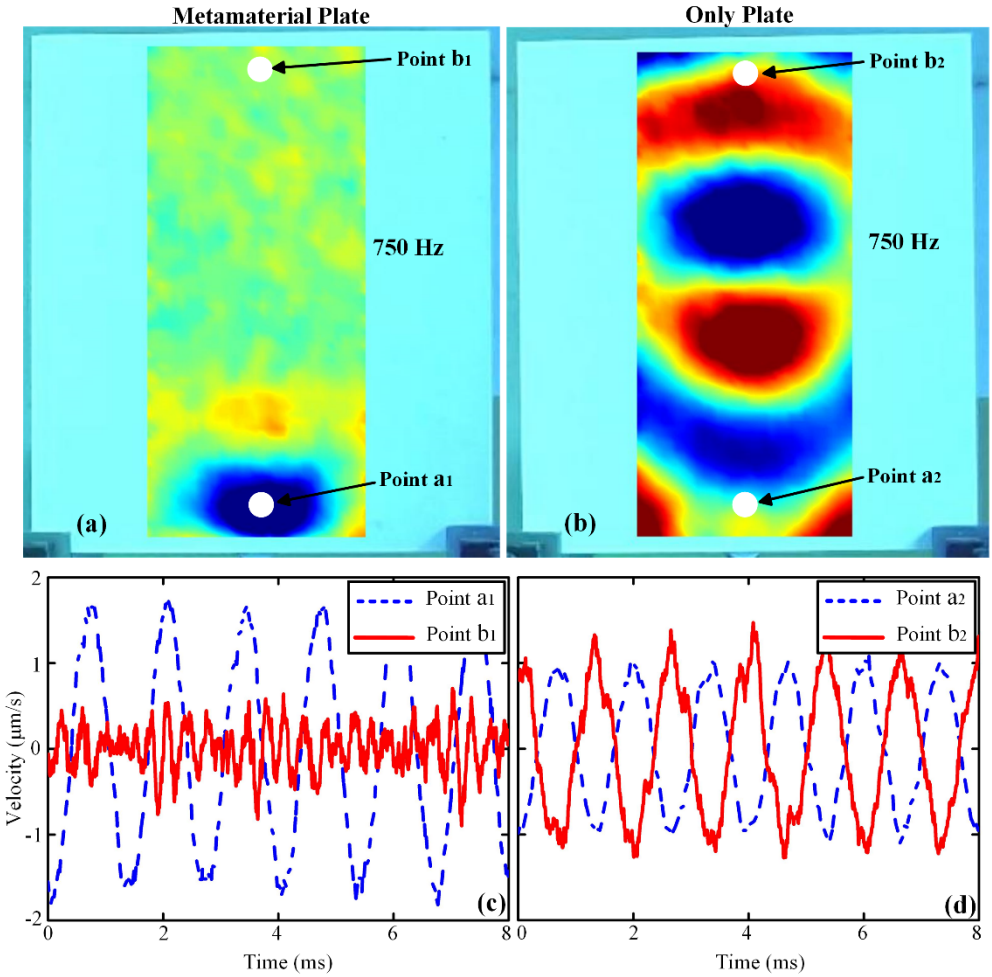

Figure 5 Experimentally measured flexural waves on the back sides of (a) the MMP and (b) the bare plate at 750 Hz. The color indicates the velocity field on the samples. (c) and (d) show the Time-Velocity curves for points a_1, b_1, a_2 and b_2 marked in (a) and (b).

It is noted that a new degree of freedom (DOF) appears because of the hinge joint, which can be used to control the position of the bandgap. Set the center position of the plate as the origin of the *x*-axis. The effects of the hinge joint's position along *x* direction on the bandgaps are shown in Fig. 6(a). The range from 200 Hz to 1800 Hz is illustrated because we focus on the lowest-frequency bandgap. The frequencies of the first and

second bandgaps increase significantly when the hinge joint moves from left to right. This is due to the fact that the magnification of inertia is constantly decreasing [48, 59].

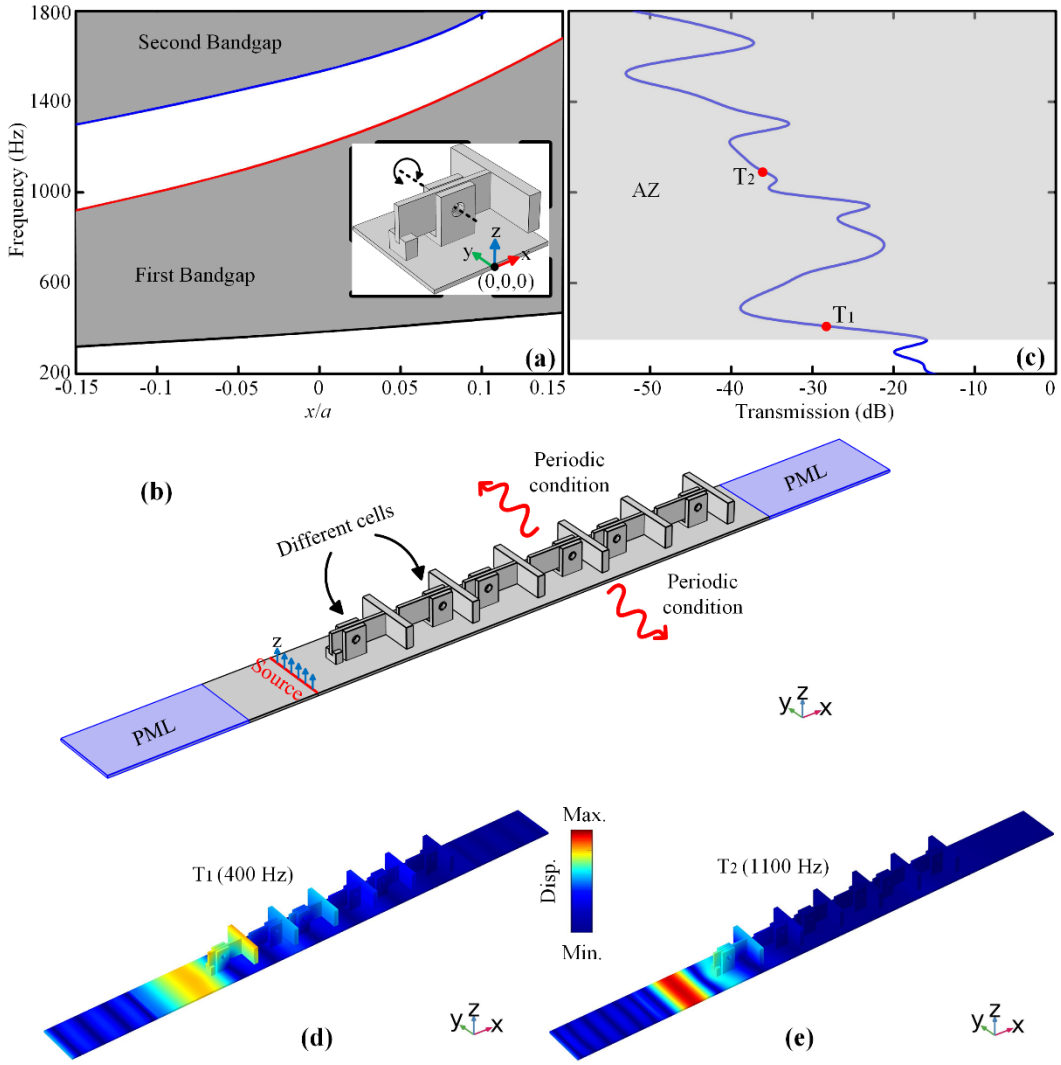

Figure 6 (a) Effects of the hinge joint's position along *x* direction on the first and second bandgaps of the MMP; (b) Schematics of the CMP and (c) the transmission of flexural waves propagating in the CMP; (d) and (e) Propagations of flexural waves in the CMP at 400 Hz (d) and 1100 Hz (e) marked as T_1 and T_2, respectively, in (c). The color bar represents the degree of the displacement. The AZ is attenuation zone.

To achieve the broadband attenuation, different kinds of unit cells are selected from Fig.

6(a) to construct a new CMP. The selected criterion is obtaining a wider AZ with minimal kinds of unit cells. Two kinds of unit cells whose hinge joints are at -0.15*a* and 0.15*a* are selected, due to the AZ of the them together is from 320 to 1800 Hz (Of course, there are many other choices). Figure 6(b) shows the schematics of the CMP. The periodic boundary conditions are applied on the edges along the *y* direction. The perfectly matched layer (PML) is utilized to reduce reflections of the free boundaries. The harmonic vibration in *z* direction on the line source is applied to achieve out-of-plane displacement in the plate. Figure 6(c) shows the transmission of the flexural waves in the range of 200 – 1800 Hz. Compared with the transmission in Fig. 3(b), the range of the AZ of the CMP is wider. Two transmission peaks can be found at 750 Hz and 950 Hz, which is due to the coupling effects between the different unit cells. We believe that more unit cells are added in the supercells, better attenuation effects and further improvement of the bandwidth we will have [63, 64].

Figures 6(d) and 6(e) show the propagations of flexural waves in the CMP at 400 Hz and 1100 Hz. These two frequencies are in the first bandgap of the MMPs whose hinge joints are at -0.15*a* and 0.15*a*, respectively. Therefore, the flexural waves can hardly travel through the CMP at these two frequencies. In addition, at high frequencies, the attenuation effects of the CMP are strong.

5. Results and Discussions of the SMs

In this section, the similar structure with inertial amplification is utilized on a soil half-space to induce low-frequency bandgap for surface waves. As we know, the artificial structure on a plate, such as the MMP, has an excellent effect in attenuating flexural

waves (out-of-plane vibration). The SMs' target is attenuation of surface waves (*xz*-plane vibration) on a half-space. Due to the huge difference between flexural waves and surface waves, the artificial structure in the MMPs that can be used to attenuate flexural waves are not necessarily suitable for a half-space to attenuate surface waves. However, some artificial structures in the MMPs can play a key role in a half-space. For instance, drilling holes periodically in a half-space [21], or burying pillars periodically in a half-space [3, 6], or erecting pillars periodically on a half-space [32, 41] all can generate bandgaps for surface waves. Moreover, some artificial structures of the MMPs covering a half-space can exert unexpected effects for surface waves. For instance, two-component [10, 65] and three-component [11] MMPs on a half space can achieve ultra-low-frequency bandgaps for surface waves. Therefore, due to the excellent performance of the lever-arm structure on the plate as shown above, we introduce it into the soil half-space to target seismic surface waves. Similar as the lever-arm structure shown in Fig. 1, the unit cell of the SM shown in Fig. 7(a) is constituted of the lever, support bar, mass, spring, hinge joint and soil substrate. Comparing with the lattice constant in Fig. 1, the lattice constant a in Fig. 7(a) is scaled to 1.5 m. The relationship between other geometric parameters and lattice constant a is consistent with those in Fig. 1. Theoretically, the depth of the half-space should be infinitely deep. In order to facilitate simulation calculations and obtain relatively accurate convergence results, the depth of the soil substrate is selected as $H = 500a$ [42, 47]. A part of the spring is replaced by a thin rubber layer with thickness of t_1 to achieve bandgaps at lower frequencies. In addition, the SM is supposed to be constructed by the ordinary building materials, for

instance, steel (mass), rubber (spring) and aluminum (support bar and lever). The material properties [6] are shown in Table 1. The mass of the steel part of the unit cell is 709.317 kg.

Table 1: The material parameters used in this paper.

Material	Density (kg/m^3)	Young's modulus (Pa)	Poisson's ratio
Steel	7784	2.07×10^{11}	0.3
Al	2700	7×10^{10}	0.33
Rubber	1300	1.2×10^{5}	0.47
Soil	1800	2×10^{7}	0.3

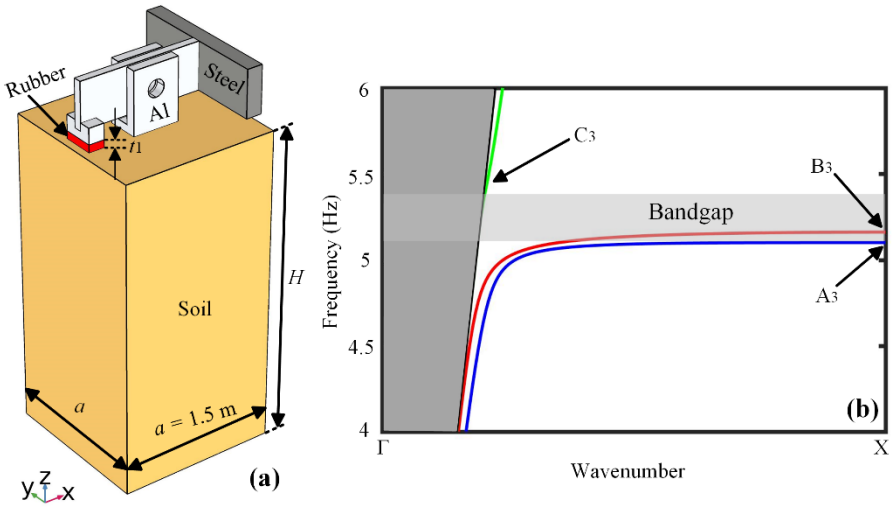

Figure 7 (a) The unit cell of the SM for surface waves. (b) The band structure of the SM for surface waves along the ΓX direction in the range from 4 Hz to 6 Hz.

Figure 7(b) shows the band structure of the SM along the ΓX direction when the thickness of the rubber is 0.02a. The area outside the dark gray area is the sound cone. Three bands can be found under the sound cone, which are illustrated by the blue, red

and green lines. A bandgap which is marked by the light gray area is shown in the frequency range from 4 Hz to 6 Hz. The transmission of the 1D periodic SM is illustrated in Appendix D. Figure 8 illustrates the vibration modes of the three points, A_3, B_3 and C_3, marked in Fig. 7(b). The central sections of these vibration modes along the *xz* plane are also provided to clearly show the effects of the inertial amplification and the characteristics of the bandgap. The arrows in Figs. 8(b), (d) and (f) indicate the displacement eigenvector; and the length and direction of the arrow indicate the magnitude and trend of the particle movement, respectively.

Figures. 8(a) and (b) show that the vibration mainly appears at the two ends of the lever which rotates around the hinge joint in the *xz* plane. This implies that the bandgap for surface waves is induced by the inertial amplification. The vibration modes illustrated in Figs. 8(c) and (d) show that there is almost no vibration in the *xz* plane. Therefore, Rayleigh waves cannot appear in the frequency range of the second band [37]. However, in the range of the third band, Rayleigh waves appear again with the particles mainly moving along *x* direction, see Figs. 8(e) and (f). So, the bandgap region shown in Fig. 7(b) for the Rayleigh waves is between the first and third bands [37].

It is known that seismic metamaterials with small mass can hardly achieve bandgaps below 10 Hz. However, the inertial amplification mechanisms with small mass can easily induce low-frequency bandgap, even for surface waves. As the first time of introducing inertial amplification mechanisms into seismic metamaterials, our goal is the existence of this bandgap rather than the enormous width of the bandgap. Therefore, we believe that narrow bandgap in this work is acceptable. To achieve the broadband

attenuation, the effects of the parameters of the hinge joint and rubber are calculated below.

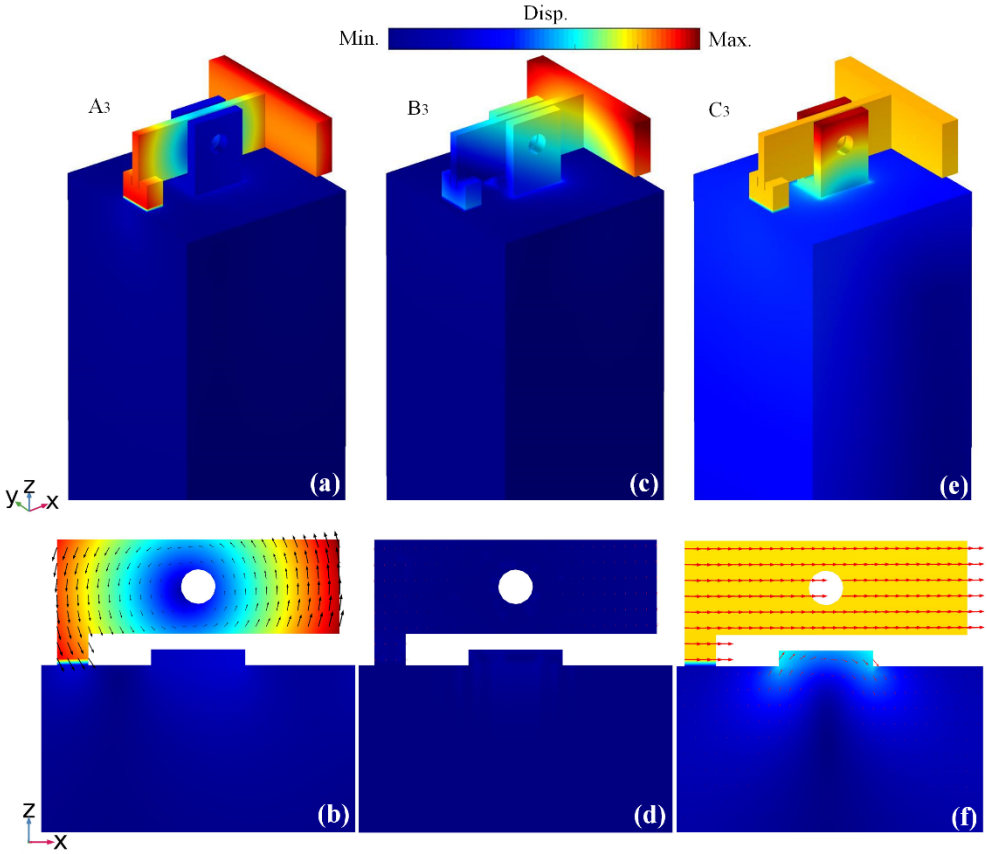

Figure 8 Vibration modes and their central section along the *xz* plane of the SM for surface waves corresponding to points (a-b) A_3, (c-d) B_3 and (e-f) C_3 marked in Fig. 7(b). The arrows in (b), (d) and (f) indicate the displacement eigenvector; and its length and direction indicate the magnitude and trend of the particle movement, respectively. The color bar represents the degree of the displacement.

The effects of the hinge joint's position, the rubber layer's thicknesses and the Young's modulus of the rubber on the bandgaps are illustrated in Fig. 9. The frequencies of the bandgap reduce significantly when the hinge joint moves from right to left along x direction. When the hinge joint moves from right to left, the μ increases and the f in Eq.

1 decreases. In addition, the frequencies of the bandgap reduce quickly when the rubber is provided, and keep decreasing when the thickness of the rubber increases. However, the relative bandwidth of the bandgap decreases with the frequency. The frequencies and the relative bandwidth of the bandgaps all increase when the Young's modulus of the rubber increases from 50 to 350 kPa. When the thickness of the rubber decreases or the Young's modulus of the rubber increases, the translational stiffness k in the vertical direction increases [25] and the f in Eq. 1 decreases.

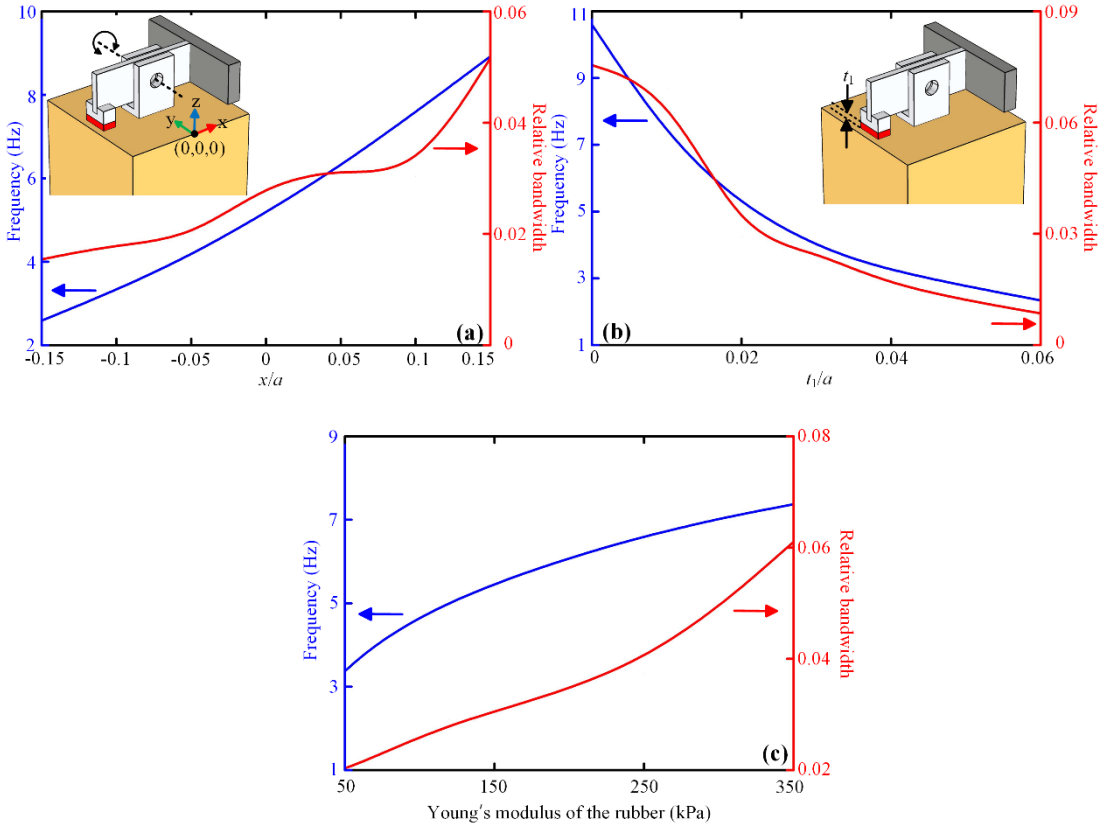

Figure 9 Effects of the hinge joint's position along x direction (a), the rubber layer's thickness (b) and the Young's modulus of the rubber (c) on the bandgaps. The blue and red solid lines are the center frequencies and relative bandwidth of the bandgaps, respectively.

Comparing with the bandgaps in Fig. 3(a) or Fig. 6(a), the bandgaps in Fig. 9 or Fig.

7(b) are narrow. This is an inevitable result. In Fig. 3(a) and Fig. 6(a), it is the flexural waves (vibration only along the z axis) that the metamaterials attenuate in a wide frequency range. In Fig. 9 and Fig. 7(b), it is the Rayleigh surface waves, which include both longitudinal (x axis) and transverse (z axis) motions, that the SMs are designed to attenuate at ultra-low frequencies. These two kinds of bandgaps cannot be directly compared. In addition, at ultra-low frequencies, the bandgap induced by inertial amplification is quite narrow, as shown in Fig. 2. Of course, the broadband attenuation effects demonstrated by using different kinds of unit cells in Figs. 6(b)-(e), can be achieved by using the SM. Suitable unit cells can be selected from Fig. 9 to construct a new seismic metamaterial to isolate seismic waves in a wide frequency range.

6. Conclusion

An alternative type of seismic metamaterial based on inertial amplification mechanism is presented in this work to open bandgaps for seismic surface waves at low frequency regime. A conceived metamaterial plate with lever-arm structures has been experimentally investigated and discussed. It is shown that a wide bandgap for flexural waves appears in a low-frequency region. The propagation analysis measured on the back side of the MMP has demonstrated that the lever-arm structures strongly attenuate the flexural waves. In addition, a new complex metamaterial plate with two kinds of unit cells has been constructed to enlarge the attenuation zone. Finally, the similar lever-arm structures are introduced into a soil half-space to obtain the bandgaps induced by inertial amplification for seismic surface waves in a low-frequency range. The

significant advantage is that inertial amplification mechanisms with small mass can achieve strong vibration attenuation at low frequencies, a property that should be realized for seismic metamaterials. Comparing with the seismic metamaterials proposed in the literature, the width of the bandgap here is not remarkable. However, since it is the first time the inertial amplification mechanism is introduced and considered in seismic metamaterials, our goal is the creation of this bandgap rather than obtaining a large width of the bandgap. Therefore, the narrow bandgap in this work is acceptable. This work provides an alternative way to control seismic surface waves at low frequencies by using a small mass. In addition, the embedded inertial amplification mechanisms have great potential to be used to attenuate seismic surface waves in a wide range at ultra-low frequencies which will be the focus of future researches.

Acknowledgements

This work is supported by la Région Grand Est, the Institut CARNOT ICEEL, and the National Natural Science Foundation of China (Grant Nos. 12021002, 12122207, 11991031, 11991032 and 41974059). The first author is grateful to the support of China Scholarship Council (Grant No. 202006250084).

Data Availability

The data that support the findings of this study are available from the corresponding author upon reasonable request.

Declaration of Competing Interest

The authors declare that they have no known competing financial interests or personal relationships that could have appeared to influence the work reported in this paper.

Appendix A. The enlarged photograph of the hinged part

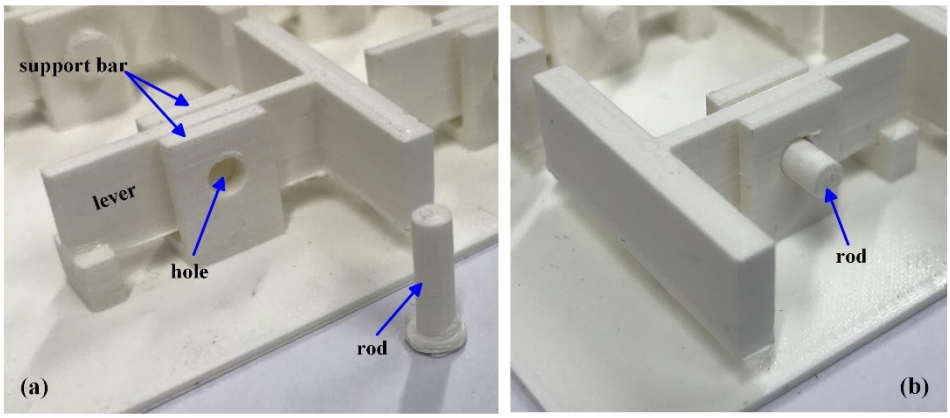

Figure A10 (a) The PLA rod, lever and support bar used at hinged part. (b) The assembled hinged part by using lever, the support bar and PLA rod.

In the experiments, all parts are printed by using 3D printer. The PLA rod and the hole in the lever and the support bar shown in Fig. A10(a) are designed. The lever and the support bar are assembled with PLA rod horizontally installed through the holes to form the hinged part shown in Fig. A10(b).

Appendix B. The matrixes used in the analytical calculation

All the matrixes in the analytical calculation of the band structure of the simplified model are shown below:

$$\mathbf{H}_{1\alpha} = \begin{bmatrix} 1 & 1 & 1 & 1 \\ -i\lambda & i\lambda & -\lambda & \lambda \\ -EI\lambda^2 & EI\lambda^2 & EI\lambda^2 & EI\lambda^2 \\ -iEI\lambda^3 & iEI\lambda^3 & EI\lambda^3 & -EI\lambda^3 \end{bmatrix},$$

$$\mathbf{H}_{1\beta} = \begin{bmatrix} e^{-i\lambda l_2} & e^{i\lambda l_2} & e^{-\lambda l_2} & e^{\lambda l_2} \\ -i\lambda e^{-i\lambda l_2} & i\lambda e^{i\lambda l_2} & -\lambda e^{-\lambda l_2} & \lambda e^{\lambda l_2} \\ -EI\lambda^2 e^{-i\lambda l_2} & -EI\lambda^2 e^{i\lambda l_2} & EI\lambda^2 e^{-\lambda l_2} & EI\lambda^2 e^{\lambda l_2} \\ -iEI\lambda^3 e^{-i\lambda l_2} & iEI\lambda^3 e^{i\lambda l_2} & EI\lambda^3 e^{-\lambda l_2} & -EI\lambda^3 e^{\lambda l_2} \end{bmatrix},$$

$$\mathbf{H}_1 = \mathbf{H}_{1\beta}\mathbf{H}_{1\alpha}^{-1},$$

$$\mathbf{H}_{2\alpha} = \mathbf{H}_{1\beta},$$

$$\mathbf{H}_{2\beta} = \begin{bmatrix} e^{-i\lambda a} & e^{i\lambda a} & e^{-\lambda a} & e^{\lambda a} \\ -i\lambda e^{-i\lambda a} & i\lambda e^{i\lambda a} & -\lambda e^{-\lambda a} & \lambda e^{\lambda a} \\ -EI\lambda^2 e^{-i\lambda a} & -EI\lambda^2 e^{i\lambda a} & EI\lambda^2 e^{-\lambda a} & EI\lambda^2 e^{\lambda a} \\ -iEI\lambda^3 e^{-i\lambda a} & iEI\lambda^3 e^{i\lambda a} & EI\lambda^3 e^{-\lambda a} & -EI\lambda^3 e^{\lambda a} \end{bmatrix},$$

$$\mathbf{H}_2 = \mathbf{H}_{2\beta}\mathbf{H}_{2\alpha}^{-1},$$

$$\mathbf{H}_3 = \begin{bmatrix} 1 & 0 & 0 & 0 \\ 0 & 1 & 0 & 0 \\ 0 & 0 & 1 & 0 \\ -G_1 & 0 & 0 & 1 \end{bmatrix},$$

$$\mathbf{H}_4 = \begin{bmatrix} 0 & 0 & 0 & 0 \\ 0 & 0 & 0 & 0 \\ 0 & 0 & 0 & 0 \\ G_1 & 0 & 0 & 0 \end{bmatrix},$$

$$\mathbf{H}_5 = \begin{bmatrix} 1 & 0 & 0 & 0 \\ 0 & 1 & 0 & 0 \\ 0 & 0 & 1 & 0 \\ G_2 & 0 & 0 & 1 \end{bmatrix},$$

$$\mathbf{H}_6 = \begin{bmatrix} 0 & 0 & 0 & 0 \\ 0 & 0 & 0 & 0 \\ 0 & 0 & 0 & 0 \\ -G_2 & 0 & 0 & 0 \end{bmatrix}.$$

Appendix C. The vibration modes at 2nd and 3rd bands in Fig. 3(a)

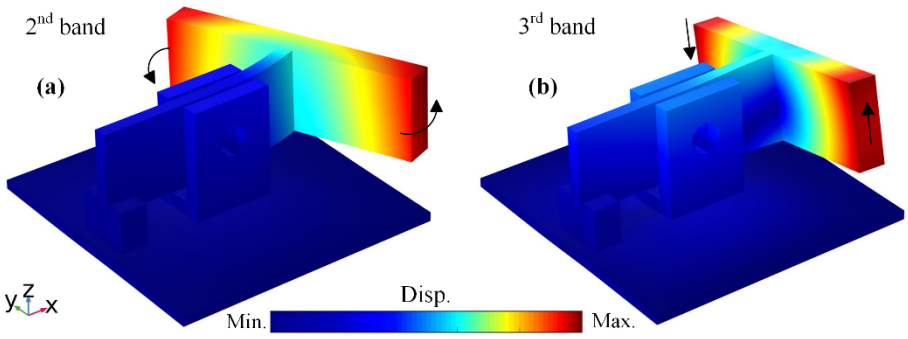

Figure A11 The vibration modes at (a) 2nd and (b) 3rd bands in Fig. 3(a).

The vibration modes at second and third bands are illustrated in Fig. A11. At second band, shown in Fig. A11(a), the mass is rotating resonance in *xy* plane. At third band, shown in Fig. A11(b), the mass is rotating resonance in *yz* plane. It is worth noting that these two kinds of local resonances are hard to be excited by flexural waves. It also demonstrates why there is no sign of these two bands in the simulated and experimental

transmission results.

Appendix D. 1D periodic seismic metamaterial

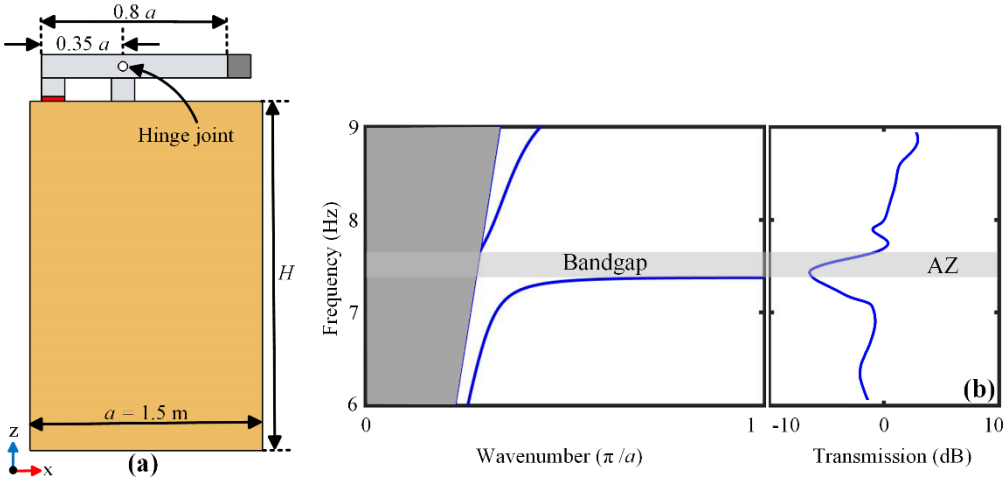

Figure A12 (a)The unit cell, (b) band structure and transmission of the 1D seismic metamaterial.

Figure A12 shows the unit cell, band structure and transmission of the 1D seismic metamaterial. Similar as the unit cell shown in Fig. 7(a), the yellow, red, silver and dark grey parts are soil, rubber, aluminum and steel, respectively. The lattice constant a is 1.5 m. The depth of the substrate H is 500a. The thickness of the rubber is 0.02a. The size of the steel is 0.1a * 0.1a. The length of the lever l_1 and the distance between the spring and support bar l_2 are 0.8a and 0.35a, respectively. 10 unit cells are used to calculated the transmission curve. The band structure and transmission show the bandgap and attenuation zone around 7.5 Hz.

References

[1] C. Arnold, EARTHQUAKE EFFECTS ON BUILDINGS 4, Des. Earthquakes, A Man. Archit., Federal Emergency Management Agency, (2006).

[2] S.-H. Kim, M.P. Das, Artificial seismic shadow zone by acoustic metamaterials, Modern Physics Letters B, 27 (2013) 1350140.

[3] S. Brûlé, E. Javelaud, S. Enoch, S. Guenneau, Experiments on seismic metamaterials: Molding surface waves, Physical Review Letters, 112 (2014) 133901.

[4] G. Finocchio, O. Casablanca, G. Ricciardi, U. Alibrandi, F. Garescì, M. Chiappini, B. Azzerboni,

Seismic metamaterials based on isochronous mechanical oscillators, Applied Physics Letters, 104 (2014) 191903.
[5] N. Aravantinos-Zafiris, M. Sigalas, Large scale phononic metamaterials for seismic isolation, Journal of Applied Physics, 118 (2015) 064901.
[6] M. Miniaci, A. Krushynska, F. Bosia, N.M. Pugno, Large scale mechanical metamaterials as seismic shields, New Journal of Physics, 18 (2016) 083041.
[7] A. Colombi, P. Roux, S. Guenneau, P. Gueguen, R.V. Craster, Forests as a natural seismic metamaterial: Rayleigh wave bandgaps induced by local resonances, Scientific Reports, 6 (2016) 19238.
[8] A. Colombi, D. Colquitt, P. Roux, S. Guenneau, R.V. Craster, A seismic metamaterial: The resonant metawedge, Scientific Reports, 6 (2016) 27717.
[9] Y. Achaoui, T. Antonakakis, S. Brûlé, R.V. Craster, S. Enoch, S. Guenneau, Clamped seismic metamaterials: ultra-low frequency stop bands, New Journal of Physics, 19 (2017) 063022.
[10] Y. Zeng, Y. Xu, K. Deng, P. Peng, H. Yang, M. Muzamil, Q. Du, A broadband seismic metamaterial plate with simple structure and easy realization, Journal of Applied Physics, 125 (2019) 224901.
[11] Y. Zeng, P. Peng, Q.-J. Du, Y.-S. Wang, B. Assouar, Subwavelength seismic metamaterial with an ultra-low frequency bandgap, Journal of Applied Physics, 128 (2020) 014901.
[12] Z. Liu, X. Zhang, Y. Mao, Y. Zhu, Z. Yang, C. Chan, P. Sheng, Locally resonant sonic materials, Science, 289 (2000) 1734-1736.
[13] T.-T. Wu, L.-C. Wu, Z.-G. Huang, Frequency band-gap measurement of two-dimensional air/silicon phononic crystals using layered slanted finger interdigital transducers, Journal of Applied Physics, 97 (2005) 094916.
[14] V. Laude, M. Wilm, S. Benchabane, A. Khelif, Full band gap for surface acoustic waves in a piezoelectric phononic crystal, Physical Review E, 71 (2005) 036607.
[15] Y. Ding, Z. Liu, C. Qiu, J. Shi, Metamaterial with simultaneously negative bulk modulus and mass density, Physical Review Letters, 99 (2007) 093904.
[16] J. Gao, X.-Y. Zou, J.-C. Cheng, B. Li, Band gaps of lower-order Lamb wave in thin plate with one-dimensional phononic crystal layer: Effect of substrate, Applied Physics Letters, 92 (2008) 023510.
[17] G. Ma, C. Fu, G. Wang, P. Del Hougne, J. Christensen, Y. Lai, P. Sheng, Polarization bandgaps and fluid-like elasticity in fully solid elastic metamaterials, Nature communications, 7 (2016) 13536.
[18] A. Colombi, R.V. Craster, D. Colquitt, Y. Achaoui, S. Guenneau, P. Roux, M. Rupin, Elastic wave control beyond band-gaps: shaping the flow of waves in plates and half-spaces with subwavelength resonant rods, Frontiers in Mechanical Engineering, 3 (2017) 10.
[19] S. An, H. Shu, S. Liang, X. Shi, Z. Lei, Band gap characteristics of radial wave in a two-dimensional cylindrical shell with radial and circumferential periodicities, AIP Advances, 8 (2018) 035110.
[20] Y.-F. Wang, Y.-Z. Wang, B. Wu, W. Chen, Y.-S. Wang, Tunable and Active Phononic Crystals and Metamaterials, Applied Mechanics Reviews, 72 (2020) 040801.
[21] F. Meseguer, M. Holgado, D. Caballero, N. Benaches, J. Sánchez-Dehesa, C. López, J. Llinares, Rayleigh-wave attenuation by a semi-infinite two-dimensional elastic-band-gap crystal, Physical Review B, 59 (1999) 12169.
[22] B. Graczykowski, F. Alzina, J. Gomis-Bresco, C. Sotomayor Torres, Finite element analysis of

true and pseudo surface acoustic waves in one-dimensional phononic crystals, Journal of Applied Physics, 119 (2016) 025308.
[23] A. Diatta, Y. Achaoui, S. Brûlé, S. Enoch, S. Guenneau, Control of Rayleigh-like waves in thick plate Willis metamaterials, AIP Advances, 6 (2016) 121707.
[24] Y. Achaoui, B. Ungureanu, S. Enoch, S. Brûlé, S. Guenneau, Seismic waves damping with arrays of inertial resonators, Extreme Mechanics Letters, 8 (2016) 30-37.
[25] A. Palermo, S. Krödel, A. Marzani, C. Daraio, Engineered metabarrier as shield from seismic surface waves, Scientific reports, 6 (2016) 39356.
[26] S. Brule, S. Enoch, S. Guenneau, Experimental evidence of auxetic features in seismic metamaterials: Ellipticity of seismic Rayleigh waves for subsurface architectured ground with holes, arXiv preprint arXiv:1809.05841, (2018).
[27] A. Palermo, M. Vitali, A. Marzani, Metabarriers with multi-mass locally resonating units for broad band Rayleigh waves attenuation, Soil Dynamics and Earthquake Engineering, 113 (2018) 265-277.
[28] Y. Zeng, Y. Xu, K. Deng, Z. Zeng, H. Yang, M. Muzamil, Q. Du, Low-frequency broadband seismic metamaterial using I-shaped pillars in a half-space, Journal of Applied Physics, 123 (2018) 214901.
[29] W. Liu, G.H. Yoon, B. Yi, Y. Yang, Y. Chen, Ultra-wide band gap metasurfaces for controlling seismic surface waves, Extreme Mechanics Letters, 41 (2020) 101018.
[30] S.-Y. Zhang, D.-J. Yan, Y.-S. Wang, Y.-F. Wang, V. Laude, Wave propagation in one-dimensional fluid-saturated porous phononic crystals with partial-open pore interfaces, International Journal of Mechanical Sciences, 195 (2021) 106227.
[31] Z. Liu, K.-Q. Qin, G.-L. Yu, Partially Embedded Gradient Metabarrier: Broadband Shielding from Seismic Rayleigh Waves at Ultralow Frequencies, Journal of Engineering Mechanics, 146 (2020) 04020032.
[32] S. Brûlé, E.H. Javelaud, S. Enoch, S. Guenneau, Flat lens effect on seismic waves propagation in the subsoil, Scientific reports, 7 (2017) 18066.
[33] D. Colquitt, A. Colombi, R. Craster, P. Roux, S. Guenneau, Seismic metasurfaces: Sub-wavelength resonators and Rayleigh wave interaction, Journal of the Mechanics and Physics of Solids, 99 (2017) 379-393.
[34] X. Pu, A. Palermo, Z. Cheng, Z. Shi, A. Marzani, Seismic metasurfaces on porous layered media: Surface resonators and fluid-solid interaction effects on the propagation of Rayleigh waves, International Journal of Engineering Science, 154 (2020) 103347.
[35] Y. Yan, A. Laskar, Z. Cheng, F. Menq, Y. Tang, Y. Mo, Z. Shi, Seismic isolation of two dimensional periodic foundations, Journal of Applied Physics, 116 (2014) 044908.
[36] O. Casablanca, G. Ventura, F. Garescì, B. Azzerboni, B. Chiaia, M. Chiappini, G. Finocchio, Seismic isolation of buildings using composite foundations based on metamaterials, Journal of Applied Physics, 123 (2018) 174903.
[37] Q. Du, Y. Zeng, Y. Xu, H. Yang, Z. Zeng, H-fractal seismic metamaterial with broadband low-frequency bandgaps, Journal of Physics D: Applied Physics, 51 (2018) 105104.
[38] P. Roux, D. Bindi, T. Boxberger, A. Colombi, F. Cotton, I. Douste-Bacque, S. Garambois, P. Gueguen, G. Hillers, D. Hollis, Toward seismic metamaterials: The METAFORET project, Seismological Research Letters, 89 (2018) 582-593.
[39] Y. Chen, Q. Feng, F. Scarpa, L. Zuo, X. Zhuang, Harnessing multi-layered soil to design seismic

metamaterials with ultralow frequency band gaps, Materials & Design, (2019) 107813.
[40] C. Lim, J. Reddy, Built-up structural steel sections as seismic metamaterials for surface wave attenuation with low frequency wide bandgap in layered soil medium, Engineering Structures, 188 (2019) 440-451.
[41] Y. Zeng, Y. Xu, H. Yang, M. Muzamil, R. Xu, K. Deng, P. Peng, Q. Du, A Matryoshka-like seismic metamaterial with wide band-gap characteristics, International Journal of Solids and Structures, 185-186 (2020) 334-341.
[42] Y. Zeng, S.-Y. Zhang, H.-T. Zhou, Y.-F. Wang, L. Cao, Y. Zhu, Q.-J. Du, B. Assouar, Y.-S. Wang, Broadband inverted T-shaped seismic metamaterial, Materials & Design, 208 (2021) 109906.
[43] Q. Gan, Y. Gao, K. Wagner, D. Vezenov, Y.J. Ding, F.J. Bartoli, Experimental verification of the rainbow trapping effect in adiabatic plasmonic gratings, Proceedings of the National Academy of Sciences, 108 (2011) 5169-5173.
[44] H. Hu, D. Ji, X. Zeng, K. Liu, Q. Gan, Rainbow trapping in hyperbolic metamaterial waveguide, Scientific reports, 3 (2013) 1249.
[45] S. Krödel, N. Thomé, C. Daraio, Wide band-gap seismic metastructures, Extreme Mechanics Letters, 4 (2015) 111-117.
[46] X. Wu, Z. Wen, Y. Jin, T. Rabczuk, X. Zhuang, B. Djafari-Rouhani, Broadband Rayleigh wave attenuation by gradient metamaterials, International Journal of Mechanical Sciences, (2021) 106592.
[47] Y. Zeng, L. Cao, Y. Zhu, Y.-F. Wang, Q.-J. Du, Y.-S. Wang, B. Assouar, Coupling the first and second attenuation zones in seismic metasurface, Applied Physics Letters, 119 (2021) 013501.
[48] C. Yilmaz, N. Kikuchi, Analysis and design of passive low-pass filter-type vibration isolators considering stiffness and mass limitations, Journal of sound and vibration, 293 (2006) 171-195.
[49] C. Yilmaz, G.M. Hulbert, N. Kikuchi, Phononic band gaps induced by inertial amplification in periodic media, Physical Review B, 76 (2007) 054309.
[50] C. Yilmaz, G. Hulbert, Theory of phononic gaps induced by inertial amplification in finite structures, Physics Letters A, 374 (2010) 3576-3584.
[51] J. Li, S. Li, Generating ultra wide low-frequency gap for transverse wave isolation via inertial amplification effects, Physics Letters A, 382 (2018) 241-247.
[52] N.M. Frandsen, O.R. Bilal, J.S. Jensen, M.I. Hussein, Inertial amplification of continuous structures: Large band gaps from small masses, Journal of Applied Physics, 119 (2016) 124902.
[53] G. Acar, C. Yilmaz, Experimental and numerical evidence for the existence of wide and deep phononic gaps induced by inertial amplification in two-dimensional solid structures, Journal of Sound and Vibration, 332 (2013) 6389-6404.
[54] S. Taniker, C. Yilmaz, Design, analysis and experimental investigation of three-dimensional structures with inertial amplification induced vibration stop bands, International Journal of Solids and Structures, 72 (2015) 88-97.
[55] O. Yuksel, C. Yilmaz, Realization of an ultrawide stop band in a 2-d elastic metamaterial with topologically optimized inertial amplification mechanisms, International Journal of Solids and Structures, 203 (2020) 138-150.
[56] K. Mizukami, K. Funaba, K. Ogi, Design and three-dimensional printing of carbon-fiber-composite elastic metamaterials with inertial amplification mechanisms, Journal of Sound and Vibration, 513 (2021) 116412.
[57] A.H. Orta, C. Yilmaz, Inertial amplification induced phononic band gaps generated by a

compliant axial to rotary motion conversion mechanism, Journal of Sound and Vibration, 439 (2019) 329-343.
[58] C. Xi, L. Dou, Y. Mi, H. Zheng, Inertial amplification induced band gaps in corrugated-core sandwich panels, Composite Structures, 267 (2021) 113918.
[59] S. Wang, M. Wang, Z. Guo, Adjustable low-frequency bandgap of flexural wave in an Euler-Bernoulli meta-beam with inertial amplified resonators, Physics Letters A, 417 (2021) 127671.
[60] L. Cao, Y. Zhu, Y. Xu, S.-W. Fan, Z. Yang, B. Assouar, Elastic Bound State in the Continuum with Perfect Mode Conversion, Journal of the Mechanics and Physics of Solids, (2021) 104502.
[61] L. Cao, Z. Yang, Y. Xu, Z. Chen, Y. Zhu, S.-W. Fan, K. Donda, B. Vincent, B. Assouar, Pillared elastic metasurface with constructive interference for flexural wave manipulation, Mechanical Systems and Signal Processing, 146 (2021) 107035.
[62] Y. Liu, D. Yu, L. Li, H. Zhao, J. Wen, X. Wen, Design guidelines for flexural wave attenuation of slender beams with local resonators, Physics Letters A, 362 (2007) 344-347.
[63] K. Donda, Y. Zhu, S.-W. Fan, L. Cao, Y. Li, B. Assouar, Extreme low-frequency ultrathin acoustic absorbing metasurface, Applied Physics Letters, 115 (2019) 173506.
[64] L. Quan, A. Alù, Passive acoustic metasurface with unitary reflection based on nonlocality, Physical Review Applied, 11 (2019) 054077.
[65] X. Wang, S. Wan, Y. Nian, P. Zhou, Y. Zhu, Periodic in-filled pipes embedded in semi-infinite space as seismic metamaterials for filtering ultra-low-frequency surface waves, Construction and Building Materials, 313 (2021) 125498.